Spatially-Resolved Mid-Infrared Spectral Evidence of Space Weathering

K. L. Utt[1], R. C. Ogliore[1], H. A.Bechtel[2], J. J. Gillis-Davis[1], and B. L. Jolliff[3,4]

[1]Department of Physics, Washington University in St. Louis, St. Louis, MO, USA
[2]Advanced Light Source Division, Lawrence Berkeley National Laboratory, Berkeley, CA, USA
[3]Department of Earth and Planetary Sciences, Washington University in St. Louis, St. Louis, MO, USA
[4]McDonnell Center for the Space Sciences, Washington University in St. Louis, St. Louis, MO, USA

Key Points:

- Lunar soils were studied with spatially-resolved near-field spectroscopy in the mid-infrared
- Spectral effects of space weathering were observed to vary continuously over a depth of 500 nm
- Direct experimental evidence supports a connection between microstructural/chemical changes and mid-infrared effects in weathered lunar soil

Corresponding author: Kainen Utt, k.l.utt@wustl.edu

Abstract

Space weathering processes induce changes to the physical, chemical, and optical properties of space-exposed soil grains. For the Moon, space weathering causes reddening, darkening, and diminished contrast in reflectance spectra over visible and near-infrared wavelengths. The physical and chemical changes responsible for these optical effects occur on scales below the diffraction limit of traditional far-field spectroscopic techniques. Recently developed super-resolution spectroscopic techniques provide an opportunity to understand better the optical effects of space weathering on the sub-micrometer length scale. In this paper, we used a synchrotron-based spectroscopic technique with ∼20 nm spatial resolution to examine cross-sections from two mature lunar soils at mid-infrared wavelengths (700–2000 cm^{-1}; 5–14.3 µm). Our findings are broadly consistent with prior bulk observations and theoretical models of space weathered spectra of lunar materials. These results provide a direct spatial link between the physical/chemical changes in space-exposed grain surfaces and spectral changes of space-weathered bodies.

Plain Language Summary

The surface of the Moon, unprotected from the space environment, is bombarded with solar wind ions and micrometeoroids. These interactions are part of a process known as space weathering, which changes the physical and optical properties of lunar soils, as well as asteroid surfaces, on a microscopic scale. Technological hurdles have hindered our understanding of the connection between the physical changes caused by space weathering and the optical properties thought to be a result of them. Using a new experimental technique, synchrotron infrared nano spectroscopy, we examined how various weathering processes affect the infrared spectral characteristics of lunar soil grains and how these change over different depths. With these insights, we can develop better models of space weathering to understand how different surfaces may be affected. The data from this investigation can also be used to calibrate laboratory analog studies of space weathering and to help interpret observations of bodies similar to the Moon.

1 Introduction

The Moon is subject to frequent micrometeoroid impacts and bombardment by energetic solar wind ions. The compositional and structural changes induced by these processes on the Moon and other airless bodies are collectively referred to as space weathering (Hapke, 2001; Pieters et al., 1993). In aggregate, these changes to the morphology, chemical composition, and crystal structure of individual regolith grains alter the optical properties of the bulk soil — relative to freshly exposed lunar regolith, reflectance spectra of space exposed soils have reddened, darkened continua and weaker diagnostic absorption peaks in the visible to infrared (IR) wavelengths. These effects have also been observed in studies of S-type asteroidal surface soils (Noguchi et al., 2011, 2014) and simulated space weathering experiments (M. S. Thompson et al., 2019; Kaluna et al., 2017; Lantz et al., 2017).

The effects of space weathering occur on a spatial scale comparable to the wavelength of visible light, presenting a unique challenge to our understanding of how various weathering processes evolve and interact to produce optical changes. Nanophase iron particles, alongside other space weathering products, are localized to within 100–200 nm of the grain surface (Pieters et al., 1993, 2000; Taylor et al., 2001; Noble et al., 2005). Hence, electron microscopy techniques are well-suited to characterize microstructural and micro-compositional changes. For instance, transmission electron microscopy (TEM) of weathered lunar soils has demonstrated that many of the optical changes seen in weathered soil are associated with the presence of nanophase iron ($npFe^0$) particles in amorphous rims coating mineral grains (Keller & McKay, 1993, 1997; Taylor et al., 2001, 2010), and microphase iron that occurs in agglutinates (Basu, 2005). In particular, $npFe^0$ grains

smaller than 40 nm in diameter cause spectral reddening and darkening, while larger iron particles cause only darkening (Noble et al., 2007; Lucey & Riner, 2011). Although the physical and chemical changes caused by space weathering can be detected via TEM, the localized optical effects of these changes cannot be directly interrogated using diffraction-limited spectroscopic techniques. Traditional diffraction-limited spectroscopic techniques are unable to spatially resolve features much smaller than the wavelength of light used—most $npFe^0$ is <40 nm in diameter. Up until now, determining the cumulative effects of space weathering products on the optical properties of lunar soil has required computational modeling (Hapke, 2001; Lucey & Riner, 2011; Lucey & Noble, 2008; Wohlfarth et al., 2019).

To bridge the gap between the optical effects of space weathering and the nano-scale physio-chemical phenomena that produce them, we used Synchrotron Infrared Nano Spectroscopy (SINS) to collect IR spectral data with sub-micrometer spatial resolution from cross-sections of space-exposed lunar soil. This technique is capable of ∼20 nm spatial resolution, making it possible to assess the optical effects of weathering phenomena at a spatial resolution sufficient to resolve sub-micrometer products of lunar space weathering (Bechtel et al., 2014). This paper presents spatially-resolved evidence of space-weathering-induced changes to the optical properties of mature lunar soils in the mid-infrared (700–2000 cm^{-1}; 5–14.3 µm).

2 Materials and Methods

2.1 Sample Preparation

The examined samples were selected from fine-grained portions of mature lunar soils 79221 (I_s/FeO = 81) and 10084 (I_s/FeO = 78), shown in Fig. 1 and Fig. 2, respectively (Morris, 1978; Rhodes & Blanchard, 1982; Taylor et al., 2001). Each soil sample was secured to aluminum stubs via carbon tape and coated with ∼10 nm of gold-palladium. Target grains were imaged in secondary and backscattered electrons using a Tescan Mira3 field-emission scanning electron microscope (FEG-SEM). An EDAX energy-dispersive X-ray (EDX) spectrometer on the SEM was used for elemental analyses and mineral identification.

As described in greater detail below, SINS utilizes an atomic force microscope (AFM) tip to enhance near-field resonances at a sample surface. To interrogate changes in spectral response as a function of depth, we created thin cross-sections from the grains identified via SEM-EDX. Qualitative markers of space exposure (e.g., surface blistering, micrometeoroid impact craters, melt splash) were used to inform the site-selection for targeted liftout extraction. Cross-sections (initial thickness ≈ 1 µm) were extracted from space-exposed regions of the target grains with an FEI Quanta 3D focused ion beam (FIB) equipped with a computer-controlled Omniprobe micro-manipulator. These cross-sections were transferred to an Omniprobe lift-out grid, upon which they were thinned to 300–600 nm thick and polished with a low-energy (5 kV, 48 pA) Ga^+ beam. The thinned sections were then placed onto an ultra-flat (surface roughness < 0.5 nm) Si chip. Using an ultra-flat Si substrate served the dual purposes of minimizing damage to the AFM tip during measurement and acting as a spectral background to which sample spectra could be referenced.

Sections 1–3 were taken from a ∼250 µm grain of 79221 with a composition consistent with anorthite-rich plagioclase (see Table 1). Section 4 was extracted from a ∼150 µm grain of 10084 with a composition consistent with Ti-, Al-rich augite, similar to that of Apollo 11 lunar rock samples (Ross et al., 1970). A fifth section was taken from a terrestrial anorthite standard (Miyake Island, Japan). The studied sections and their characteristics are outlined in Table 2.

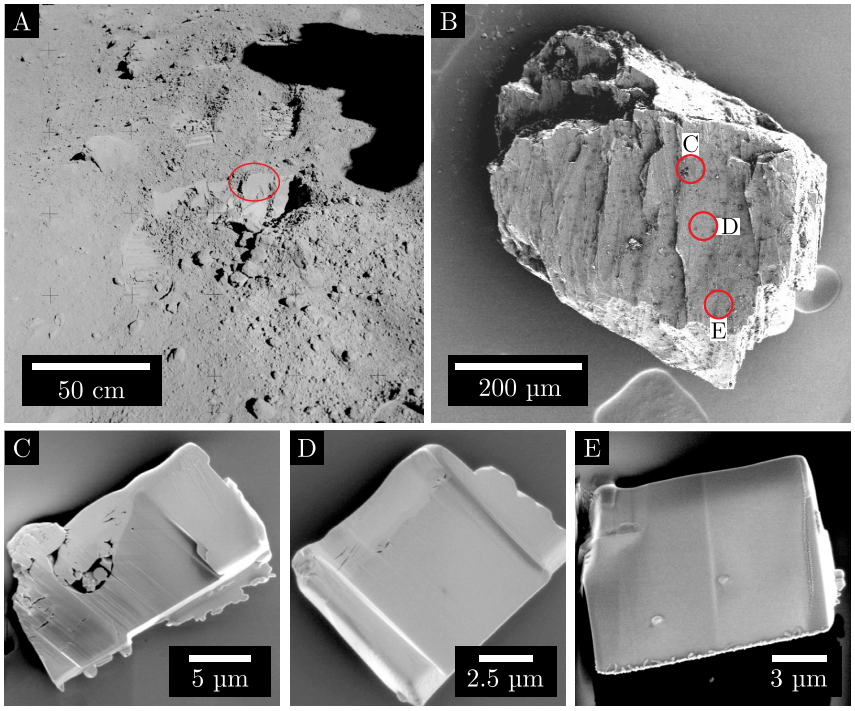

Figure 1. The geospatial context for lunar sample 79221 (Sections 1–3). **(A)** NASA photograph AS17-142-21827 showing approximate in situ sample location (circled) as recorded at the time of collection. **(B)** 2 kV SE image of target grain for sections 1–3, extracted from the circled areas. **(C)**–**(E)** 2 kV SE images of sections 1–3, respectively, on Si substrate after thinning and low-kV polishing

Table 1. SEM-EDX compositions of the studied lunar samples.

Section	Composition (atomic percent)						
	O	Mg	Al	Si	Ca	Ti	Fe
1–3	60%	—	16%	16%	8%	—	—
4	57%	6%	5%	17%	4%	3%	7%

Table 2. Descriptions of studied samples

Section	Sample	Composition	Description
1	79221	An-rich Plagioclase	Micrometeoroid impact crater
2	79221	An-rich Plagioclase	Melt-splash coated
3	79221	An-rich Plagioclase	Surface blistering
4	10084	Ti-, Al-rich Augite	Mildly amorphized surface
5	—	Anorthite	Terrestrial mineral standard

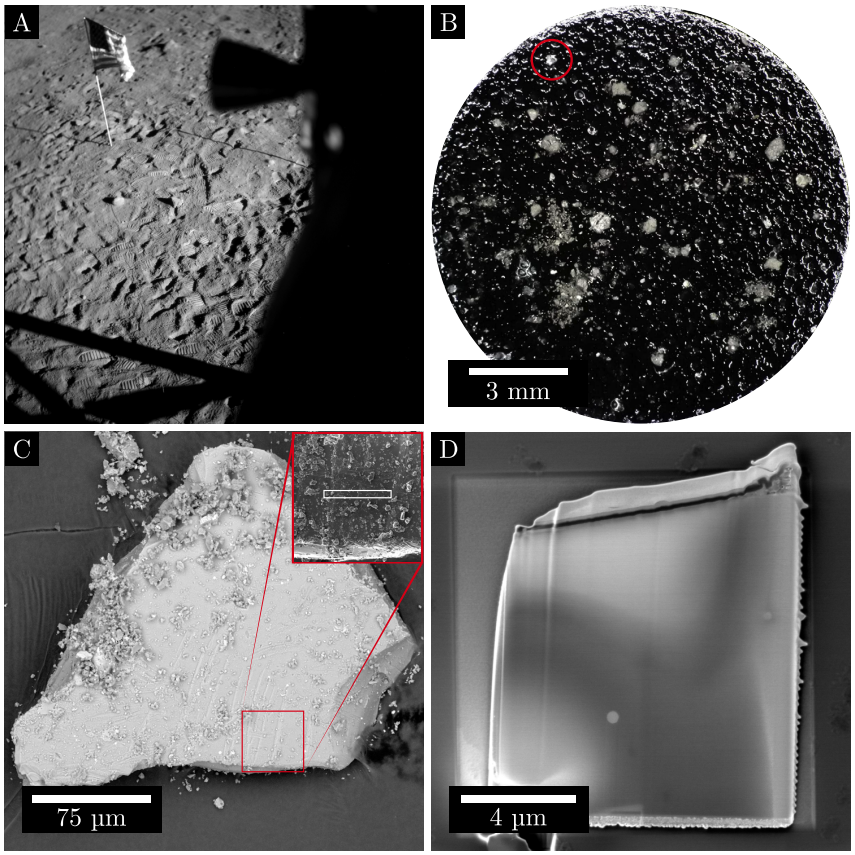

Figure 2. The geospatial context for lunar sample 10084 (Section 4). **(A)** In situ sample location as recorded from the Apollo 11 lunar module. **(B)** Optical micrograph of grains from 10084 affixed to an SEM stub with carbon tape. Section 4 was extracted from the circled grain. **(C)** Backscattered electron (BSE) image (15 kV) of the target grain for section 4 with higher-magnification secondary electron (SE) image inset. FIB extraction site for section 4 indicated by the rectangle in the inset image. **(D)** 2 kV SE image of section 4 on Si substrate after thinning and low-kV polishing by FIB.

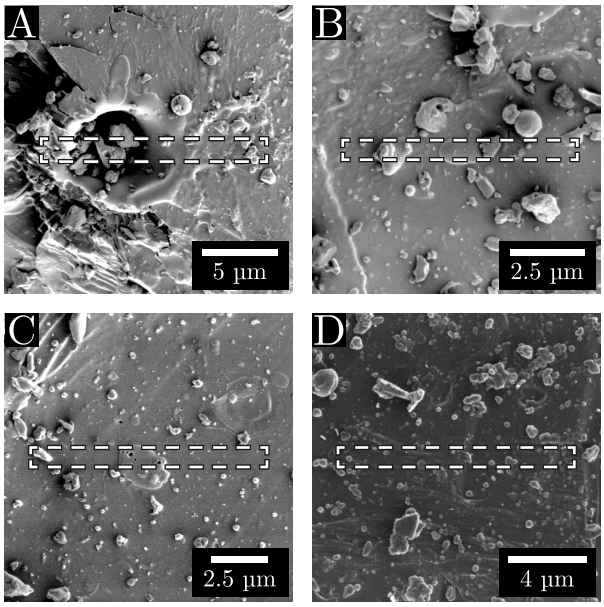

Figure 3. Close-up SE images (2 kV) of the selected FIB extraction sites shown in Figure 1B and Figure 2C. The area sampled by each cross-section is indicated by a dashed rectangle. **(A)** Hypervelocity micrometeoroid impact crater sampled by section 1 (79221). **(B)** The site selected for section 2 (79221); displays evidence of surface blistering and includes two melt splash droplets. The left droplet contains vesiculated textures. **(C)** The extraction site for section 3 (79221) includes a vesiculated melt-splash droplet. The surface of this region of the grain displays a lesser degree of blistering than at the extraction site for section 2. **(D)** FIB extraction site for section 4 (10084), selected to include small melt splash droplets and mild surface blistering and amorphization.

2.2 Experimental Methods

Near-field IR spectra were collected using SINS at Beamline 5.4 at the Advanced Light Source (Bechtel et al., 2014). This technique can be thought of as a combination of Fourier-transform infrared spectroscopy (FTIR), scattering-type scanning optical microscopic (s-SNOM) techniques, and atomic force microscopy (AFM).

To collect SINS spectra, synchrotron IR light is coupled into an asymmetric Michelson interferometer consisting of a beamsplitter (KBr), a moving mirror (Nicolet 6700 FTIR spectrometer), and an AFM (Bruker Innova). Light is focused onto an oscillating AFM tip in one arm of the interferometer. The light scattered by the tip is combined with light reflecting off of the moving mirror in the second arm of the interferometer. The resulting interference signal is detected on a mercury cadmium telluride (HgCdTe) detector. With this experimental setup, the spatial resolution is determined by the radius of curvature of the AFM tip used (25 nm in this case) and is independent of the wavelength of incident light.

To differentiate the near-field signal from the far-field scattered background, signals are detected at higher harmonics of the tip oscillation frequency, which arise from the nonlinear near-field response. Here, we use the second harmonic response as a compromise between background suppression and signal to noise ratio. After demodulation, the interferometric signal is Fourier transformed to yield the complex near-field spectra. The spectral amplitude, $|A(\tilde{\nu})|$, relates to the real-valued component of the material's complex dielectric function (i.e., the reflection coefficient). The spectral phase, $\Phi(\tilde{\nu})$, is similarly related to the imaginary component of the dielectric function (i.e., the absorption coefficient) (Xu et al., 2012; Govyadinov et al., 2014).

Using these methods, we collected spatially-resolved spectra over a broad range of wavenumbers (700–5000 cm^{-1}). At wavenumbers greater than 2000 cm^{-1}, however, noise dominates the signal from our samples. The diamond window separating the ultra-high vacuum synchrotron storage ring from the SINS instrument has strong absorption bands at roughly 2000–2500 cm^{-1}, causing poor signal-to-noise over that range of wavenumbers and potentially obscuring any C-H stretch or O-H stretch features present in the spectra. Since the infrared spectra of plagioclase and pyroxenes contain few characteristic absorption features at wavenumbers greater than 2000 cm^{-1}, the increased noise for large wavenumbers does not present a major problem for this work. As such, the data for wavenumbers 2000–5000 cm^{-1} are omitted for clarity.

2.3 Data Analysis

The data presented in this work were processed using a custom program that employs commercially available fast Fourier Transform software packages (Wavemetrics Igor Pro). Background and instrumental responses were removed by referencing the amplitude and phase signals to a Si substrate, which yields a spectrally flat response. The referenced amplitude and phase signals were obtained via, respectively,

$$|A(\tilde{\nu})| = \frac{|A(\tilde{\nu})|_{\mathrm{sample}}}{|A(\tilde{\nu})|_{\mathrm{reference}}} \qquad \text{and} \qquad \Phi(\tilde{\nu}) = \Phi(\tilde{\nu})_{\mathrm{sample}} - \Phi(\tilde{\nu})_{\mathrm{reference}}. \tag{1}$$

Background-referenced spectra were smoothed using a robust locally estimated scatterplot smoothing (RLOESS) algorithm over a moving 75-data-point (approx. 35 cm^{-1}) window (see, e.g., Andrews, 1974; Cleveland, 1979; Cleveland & Devlin, 1988). The position of the Pt cap was determined by overlaying high-resolution SE images (in which the Pt was visually distinct from the sample) atop the AFM topographical images used for SINS target selection. Spectra collected from the Pt cap were not used for the analyses described below.

To quantify the depth-dependent changes in peak intensity, we used a custom mean-assisted peak identification and tracking algorithm. This algorithm first identifies likely peak positions (reference peaks) via comparison to the mean of the dataset, then searches for those peaks in each constituent spectrum, tracking the wavenumber and intensity at which those peaks appear. These characteristics allowed for automated processing of spectra collected via line-scans with minimal user input.

3 Results

3.1 Comparison to Terrestrial Standard

The SINS amplitude spectra from sections 1–3 are qualitatively similar to those from an identically-prepared terrestrial anorthite standard. The similarity of these spectra, shown in Fig. 4, provides evidence that SINS is sufficiently sensitive to local changes in mineral structure and chemistry. It is important to note, however, that phase spectra from section 1 share fewer similarities with those from sections 2 and 3, as well as the terrestrial standard. The two dominant features in phase spectra from the standard (Fig. 5), peaks at roughly 1000 cm^{-1} and 1150 cm^{-1}, were not observed for section 1 (Fig. 6) but can be seen for sections 2 and 3 (Figures 7 and 8, respectively). Potential explanations for this divergence are explored further in the Discussion.

The depth-dependent spectral effects seen among sections from 79221 were not observed in spectra collected from the mineral standards, indicating that they are unlikely to have arisen due to instrumental effects (see Fig. 5). Moreover, line-scans collected from the terrestrial standard at a constant depth were not found to differ from those collected at variable depths, offering supporting evidence that the observed variations are resultant of space weathering induced microstructural and chemical changes in the uppermost layers of lunar soil grains.

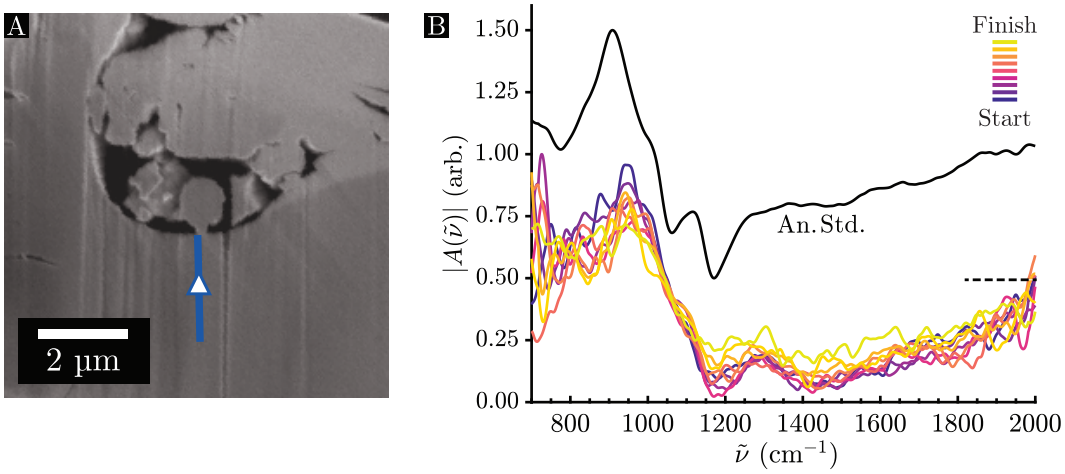

Figure 4. Comparing SINS amplitude spectra of 79221 to terrestrial anorthite (Miyake, Japan). **(A)** SE image (2 kV) of the hypervelocity impact crater sampled by section 1. The arrow indicates the location of the line-scan. **(B)** SINS amplitude spectra from a line-scan on section 1 is plotted in color, with darker colors representing spectra collected in the grain interior and lighter colors representing spectra collected at the surface. Averaged SINS amplitude spectrum for a terrestrial anorthite standard is plotted in black (offset vertically for clarity).

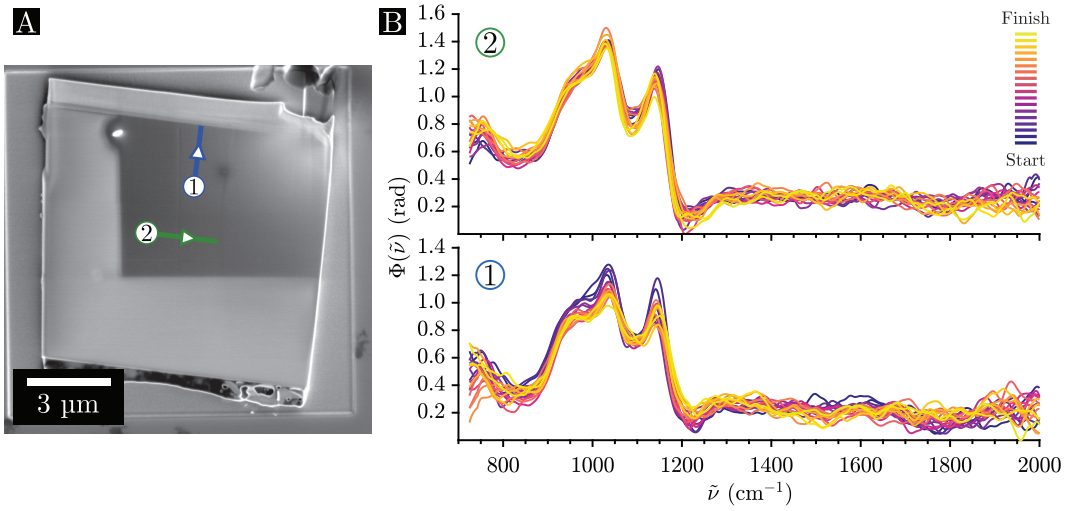

Figure 5. Line-scans collected from a terrestrial anorthite standard (Section 5). **(A)** SE image of section 5 with line-scan locations indicated. The direction of each scan is indicated with an arrow. **(B)** SINS phase spectra from the line-scans shown in (A). Spectra collected from the start of a line-scan are plotted in darker colors, whereas the lighter colors indicate spectra collected from the end of a line-scan.

3.2 Sample Phase Spectra

Many minerals have qualitatively different near-field and far-field IR spectra. Though the two spectra may share some features, there is generally not a one-to-one correlation between them (Hermann et al., 2014; Huth et al., 2012; Pollard et al., 2015). This disparity means that we cannot definitively link spectral features observed in our samples to particular vibrational modes of the crystal. Despite this, many of the features we observed in the SINS spectra of our samples are consistent with the characteristic absorption/reflectance features reported in the literature.

SINS amplitude spectra are generally more susceptible to topographical and instrumental artifacts than phase spectra. This susceptibility is in part because amplitude spectra typically present dispersive lineshapes whereas phase spectra generally occur as Gaussian or Lorentzian profiles, potentially making weak features more difficult to see in amplitude data. To examine the relative changes of particular spectral features as a function of depth, we use the phase data to maximize signal clarity.

3.2.1 Micrometeoroid Impact Crater (Section 1)

SINS phase spectra, $\Phi(\tilde{\nu})$, collected near the hypervelocity impact crater sampled by section 1 (see Fig. 3) exhibit systematic variations between the grain interior (far from the crater bottom) and the grain surface (just below the crater). Primary among these variations is the loss of spectral contrast with increasing proximity to the surface, as shown in Figure 6 and are described below.

Two peaks in the phase spectra at 1125 cm^{-1} (8.9 µm) and 1755 cm^{-1} (5.7 µm), respectively labeled as A and B in Fig. 6, broaden and display reduced spectral contrast with increasing proximity to the surface. Both peaks additionally shift to slightly lower wavenumbers at shallower depths. These effects are most notable within 300 nm of the

surface for both features. Unlike feature A, this peak (B) shifts to slightly lower wavenumbers with increasing proximity to the surface.

The broad, local maximum at 1125 cm^{-1} (A) is associated with Si-O or Al-O asymmetric stretch modes in the silicate tetrahedral structure (Johnson et al., 2003; D. Nash & Salisbury, 1991; C. S. Thompson & Wadsworth, 1957). The provenance of the feature at 1755 cm^{-1} is unclear, though it has been observed in studied of shocked terrestrial anorthite (Chihara & Koike, 2017).

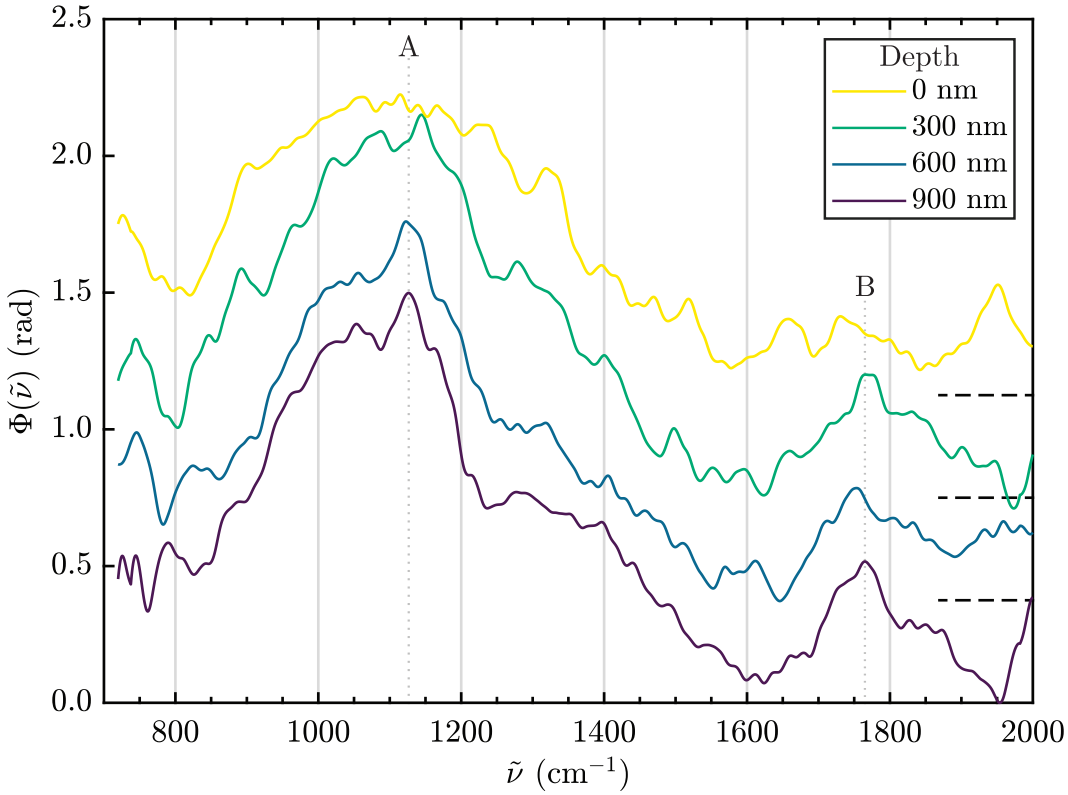

Figure 6. SINS phase spectra, $\Phi(\tilde{\nu})$, collected at the labeled distances from the bottom of the hypervelocity impact crater on the plagioclase grain sampled by section 1 (see Fig. 3A). Diminished spectral contrast was observed among spectra from close to the surface, particularly for key spectral features at 1125 cm^{-1} (8.9 µm) and 1755 cm^{-1} (5.7 µm), respectively labeled A and B.

3.2.2 Melt-Splash Coating (Section 2)

SINS phase spectra collected from section 2, which samples a melt-splash coated region approximately 150 µm from the hypervelocity impact crater sampled by Section 1 (see Fig. 3), are less noisy and contain sharper peaks than those described in 3.2.1. These spectra, shown in Figure 7, evolve as a function of depth similar to those from section 1. We observed depth-dependent loss of spectral contrast, particularly at longer wavelengths. This effect is most prominent among spectra collected from within 400 nm of the surface.

Spectra from the grain interior include a peak (labeled as A in Fig. 7) at 760 cm^{-1} (13.0 µm) that is associated with Si-Si or Si-Al stretch vibrations (Chihara & Koike, 2017;

C. S. Thompson & Wadsworth, 1957). Unlike other prominent peaks in the spectra, feature A is sharper at the surface than in the interior. A broad, minor peak (B) at 915 cm^{-1} (10.9 µm) is present in the spectrum at a depth of 1600 nm. This feature associated with Si-O asymmetric stretch vibrations does not appear in spectra from close to the surface, at which a pronounced local minimum takes its place. Two major peaks occur at 1045 cm^{-1} (9.6 µm) and 1165 cm^{-1} (8.6 µm), labeled C and D, in spectra from all sampled depths. These features are both associated with Si-O and Al-O stretch vibrations but evolve differently over depth. Feature C becomes less distinguishable from the continuum close to the surface. In contrast, feature D is substantially more prominent among spectra from the uppermost 400 nm of the sample.

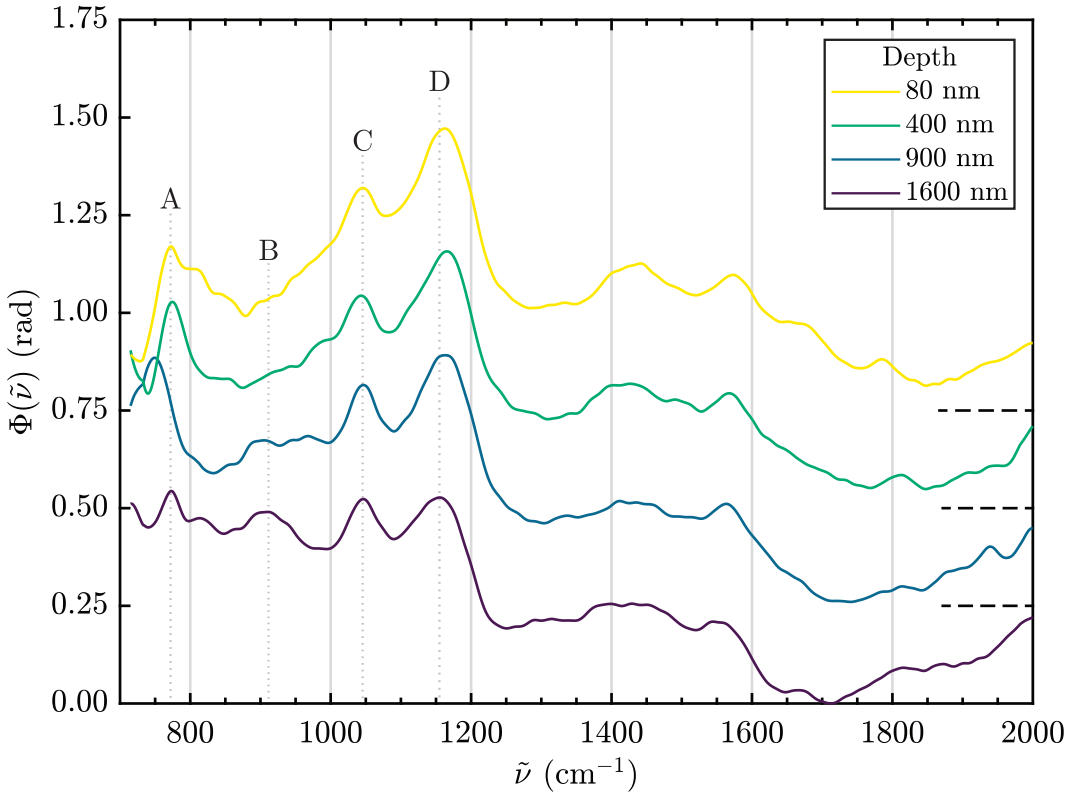

Figure 7. SINS phase spectra collected at the labeled distances from the melt-splotched surface of the plagioclase grain sampled by section 2 (see Fig. 3B). Diminished spectral contrast was observed for select features among spectra from close to the surface. Key spectral features at 770 cm^{-1}, 915 cm^{-1}, 1045 cm^{-1} and 1165 cm^{-1}, respectively labeled A–D, are discussed in greater detail in the text.

3.2.3 Surface Blistering (Section 3)

The data for section 3, which samples a region with evidence of surface blistering (see Fig. 3), have lower signal-to-noise ratios than those for sections 1 and 2. Despite the increased noise, the spectra from both Sections appear to display similar features and were observed to evolve similarly as a function of depth, as shown in Figure 8. We observed depth-dependent loss of spectral contrast, particularly in the middle of the sam-

pled wavelength range. This effect is most prominent among spectra collected from within 250 nm of the surface.

Some features of these spectra, such as the sharp peak (A) at 750 cm^{-1} (13.3 µm) associated with Si-Si stretch vibrations (Chihara & Koike, 2017; C. S. Thompson & Wadsworth, 1957), remain sharp and noticeable at all sampled depths. Others, such as a broad silicate feature (B) at 990 cm^{-1} (10.1 µm; C. S. Thompson & Wadsworth, 1957), can be seen in all spectra but are less distinguishable from the continuum within 250 nm of the surface. At 1145 cm^{-1} (8.7 µm), a small peak (C) associated with Reststrahlen absorption features and strong Si-O stretch modes (D. Nash & Salisbury, 1991) can be seen in the spectra from depths of 550 nm and 775 nm but is absent in spectra from closer to the surface. Similarly, two features (D) at 1480 cm^{-1} (6.8 µm) and 1550 cm^{-1} (6.5 µm) are distinguishable from one another in the grain interior but become indistinguishable at the surface. The pair of features at (D) is due to resonant absorption at stretch vibration modes of Si-O and Al-O bonds in the silicate framework (D. Nash & Salisbury, 1991).

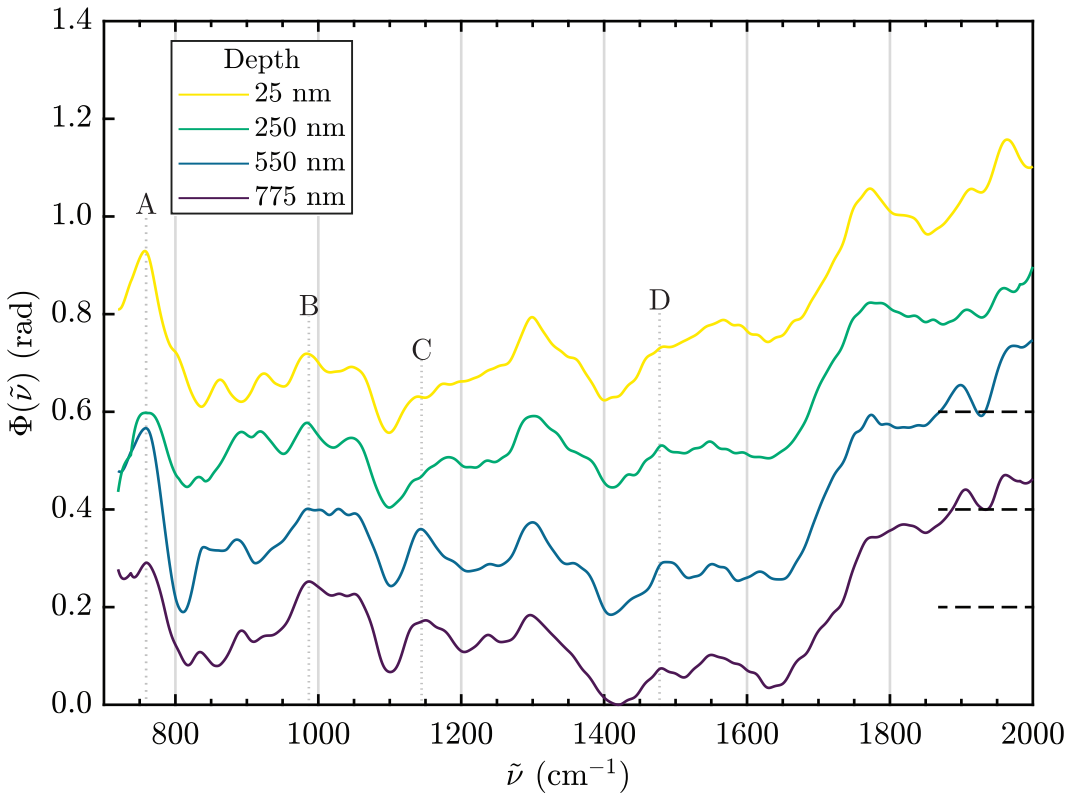

Figure 8. SINS phase spectra collected at the labeled distances from the blistered surface of the plagioclase grain sampled by section 3 (see Fig. 3C). Diminished spectral contrast was observed for all but one of the features among spectra from close to the surface. Key spectral features at 750 cm^{-1}, 990 cm^{-1}, 1145 cm^{-1}, 1480 cm^{-1} and 1550 cm^{-1}, respectively labeled A–D, are discussed in greater detail in the text.

3.2.4 Mildly Amorphous Surface (Section 4)

The spectra from section 4, shown in Fig. 9, display more subtle changes over depth compared to Sections 1–3. Potential explanations for this difference are explored in the Discussion.

Few systematic changes as a function of depth were observed at low wavenumbers ($> 1200\,\mathrm{cm}^{-1}$). There appears to be a weak feature at $750\,\mathrm{cm}^{-1}$ (13.3 µm) in spectra from depths greater than 550 nm but it is absent in spectra from closer to the surface. The dominant feature of these spectra is a large peak at roughly $1140\,\mathrm{cm}^{-1}$ (8.8 µm) associated with the first "critical absorption" feature CA1 or ν(O-Si-O) vibrational modes (Hamilton, 2000, 2003; Makreski et al., 2006). As seen in Fig. 9, this feature is unchanged over the sampled range of depths.

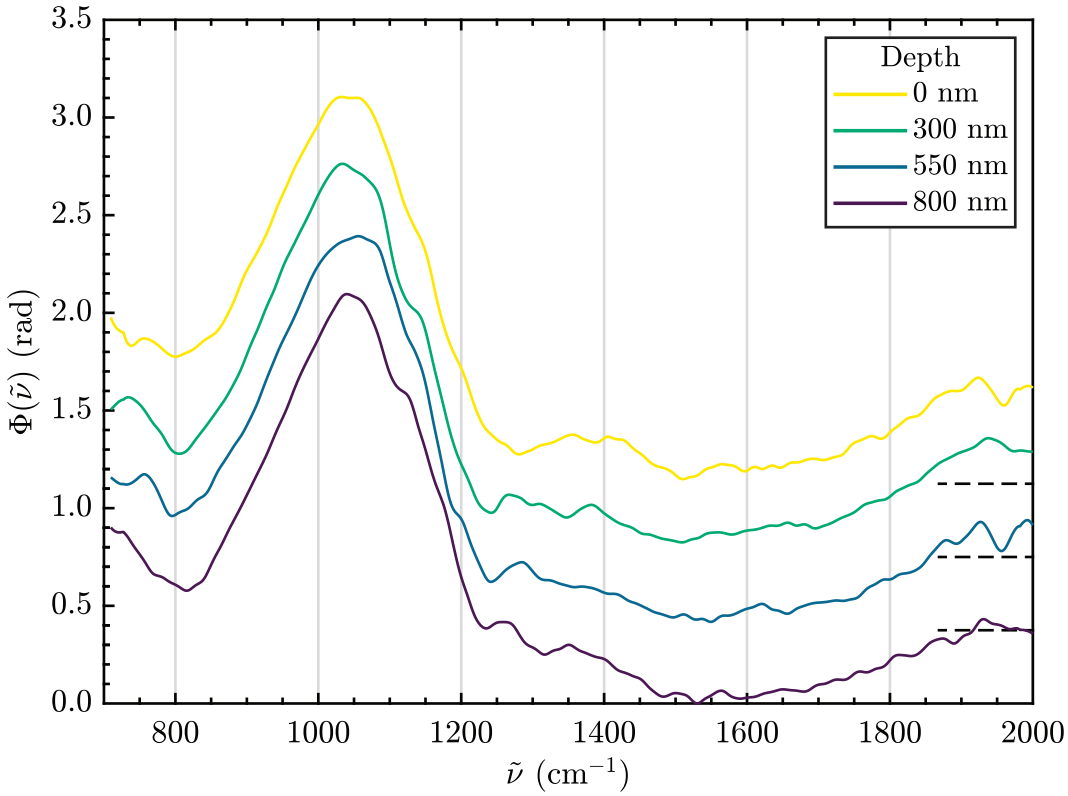

Figure 9. SINS phase spectra collected at the labeled distances from the blistered surface of the pyroxene grain sampled by section 4 (see Fig. 3D). Spectral features were not observed to undergo substantial changes over depth, as discussed in greater detail within the text.

3.3 Depth-Dependent Spectral Effects

The collected data for sections 2 and 3 indicate that peak intensity and spectral contrast are inversely correlated with distance from the space-exposed surface. Peaks present in SINS amplitude spectra from close to the surface of these two samples are significantly (∼20–80 %) less intense than in spectra collected from the crystalline grain interior (see Fig. 10). Figure 11 illustrates this effect centered about a peak at $1145\,\mathrm{cm}^{-1}$ found in the phase spectra of Section 2. In line-scans from section 2, peaks at higher wavenum-

bers were observed to be more effectively suppressed than those at lower wavenumbers. The opposite is true for sections 1 and 4. The intensity of peaks in spectra from section 4 (10084) are weakly correlated with depth, but the feature at 915 cm^{-1} is more suppressed at the surface than the feature at 1855 cm^{-1}. In line-scans from section 1, the peak at 940 cm^{-1} weakens close to the surface whereas the intensity of a peak at 1300 cm^{-1} is greater at the surface than in the grain interior.

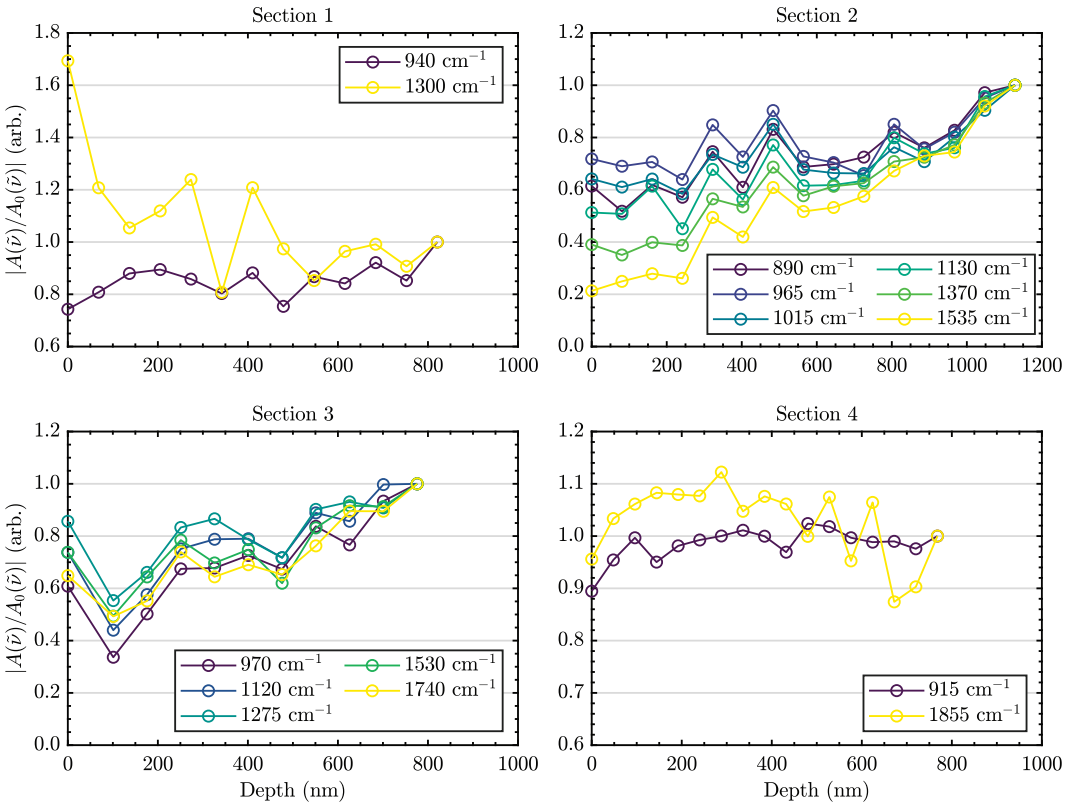

Figure 10. SINS amplitude values for diagnostic features, normalized to the grain interior, for sections 1–4. As was the case for total integrated intensity (Fig. 12), depth-dependent changes are more apparent for sections 2 and 3. Peaks from section 2 appear to be consistent with spectral reddening, since peaks at higher wavenumbers (i.e., 'bluer') are suppressed more than peaks at lower wavenumbers (i.e., 'redder').

The integrated amplitude response, analogous to total scattered intensity, was additionally observed to evolve as a function of depth (see Fig. 12). In line-scans from sections 2 and 3, total scattered intensity is strongly correlated with depth (i.e., spectra from close to the space-exposed surface are darker than those from within the grain interior). This darkening effect occurs in sections 2 and 3 over depths of 0–2000 nm, though it is most pronounced for the first 500 nm. Data from Sections 1 and 4, however, do not display a strong correlation between scattered intensity and depth.

4 Discussion

Although both soil samples are classified as 'mature' with $I_s/\mathrm{FeO} = 81$ for 79221 and $I_s/\mathrm{FeO} = 75$ for 10084 (Morris, 1978), the spectral effects of space weathering—loss of spectral contrast and broadening of absorption features—are far more pronounced among

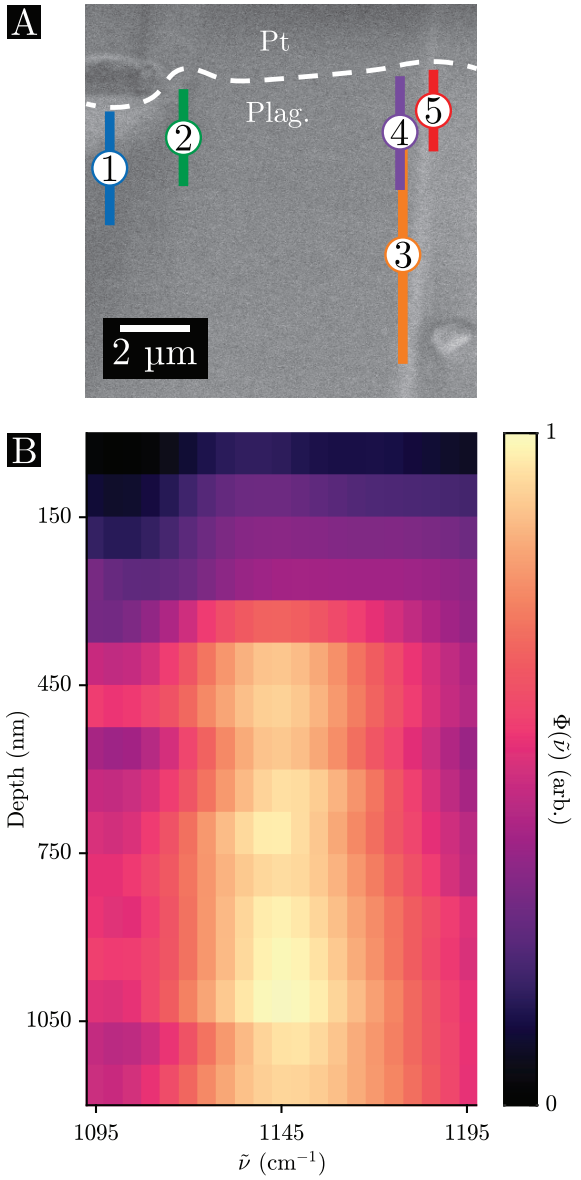

Figure 11. **(A)** SE image (2 kV) of section 3 (79221) with the locations of five line-scans superimposed. **(B)** Heatmap of SINS phase spectra from section 3 (see Fig. 8) near a peak at 1145 cm^{-1}, demonstrating a marked loss of spectral contrast within 300 nm of the space-exposed surface. The pixel color corresponds to the continuum-removed $\Phi(\tilde{\nu})$ spectra, averaged over the five line-scans shown in (A), at the given depth and wavenumber. Depth (75 nm bins) is plotted on the vertical axis. Scans were aligned such that the top of the plot corresponds to where the Pt-deposition layer begins. The wavenumber is plotted on the horizontal axis with a bin size of 5 cm^{-1}.

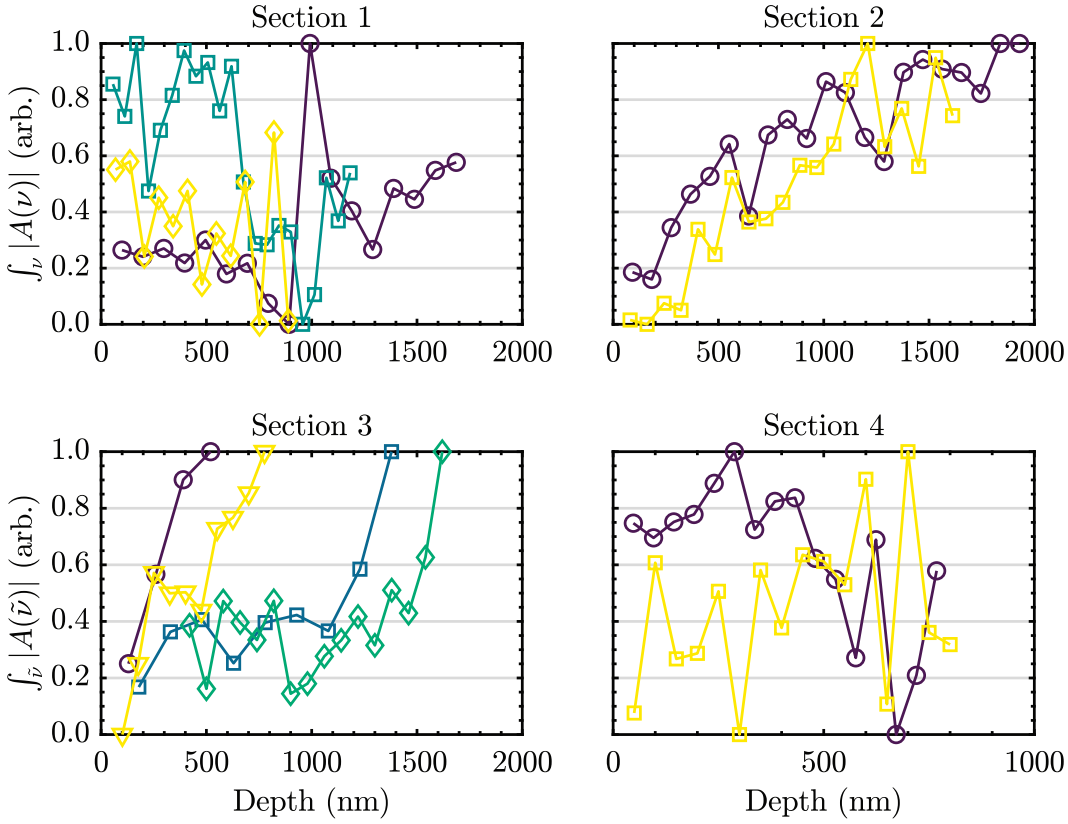

Figure 12. Integrated amplitude response (total scattered intensity, related to the reflectivity coefficient) of each line-scan as a function of distance from the space-exposed surface. Different line-scans are plotted with different colors/markers. Darkening occurs with greater proximity to the space-exposed surface in sections 2 and 3 (see Fig. 1). Section 1, which samples a hypervelocity impact crater on the same anorthite-rich plagioclase grain as sections 2 and 3, does not display the same trend. Similarly, there is not a strong correlation for section 4 (see Fig. 2).

thin-sections extracted from 79221. This observation is supported by previous shock experiments. Studies on experimentally shocked feldspars demonstrated weakening and broadening of absorption bands related to increasing glass content, particularly at shock pressures above ∼20 GPa (D. B. Nash et al., 1993; Johnson et al., 2002, 2003). In contrast, pyroxenes are more resilient to increasing shock pressures. Studies show little change in spectral properties with shock pressures of 45 GPa and up to 65 GPa (Adams et al., 1979; Johnson et al., 2002).

Shock effects may also be responsible for the apparent dissimilarity of phase spectra from section 1 and the anorthite standard. The region of the mineral grain directly below the micrometeoroid impact crater sampled by section 1 experienced much greater pressures than the material sampled by sections 2 and 3. The largest feature at roughly 1100 cm^{-1} in phase spectra from section 1 may be the result of shock-induced spectral broadening of the 1000 cm^{-1} and 1150 cm^{-1} features in the phase spectra from sections 2–3 and the anorthite standard. These differences could alternatively be explained by the presence of compositional or structural inhomogeneities in the soil grain. This interpretation could help to explain why the differences are less apparent in the amplitude data, which is less sensitive to local chemistry than the phase signal. Should this interpretation be correct, our observations serve to illustrate the value of SINS for spectroscopic investigation of micrometer-scale mineralogical variations. In this instance, the signal produced by diffraction-limited techniques be an average over various mineral structures or compositions, making it unlikely that such minor deviations in chemical composition would be detectable.

In sections 2 and 3, we observed reduced total scattered intensity with increasing proximity to the space exposed surface (see Fig. 12). This darkening is indicative of the presence of $npFe^0$ with an increasing concentration near the surface (Noble et al., 2007; Lucey & Riner, 2011). Though it is from the same soil grain as sections 2 and 3, section 1 does not exhibit a similar trend. This discrepancy indicates that there is a lower concentration of $npFe^0$ near the hypervelocity impact crater. These differences are additionally indicative of impact-induced surface amorphization and vitrification are dominant near the crater sampled by section 1 (see Fig. 6). Similarly, we did not observe a robust correlation between total scattered intensity and depth for section 4, suggesting limited concentrations of $npFe^0$.

Where present, the darkening effect is most apparent within 500 nm of the grain surface (see, e.g., Fig. 10 or Fig. 12). This depth falls just outside of the range of thicknesses for amorphous rims observed in lunar soil (∼10–350 nm (Burgess & Stroud, 2018; Christoffersen et al., 1996)), but well within the range of thicknesses for glassy silicate layers thought to have been produced by micrometeoroid impacts (10–1000 nm; Noble et al., 2005). For comparison, the average implantation depth of solar wind-produced H and He has been estimated as ∼20–100 nm (Christoffersen et al., 1996; Farrell et al., 2015; Tucker et al., 2019). That we observed space weathering effects over a broader range of depths than the depth-distribution of implanted hydrogen points towards a more continuous, perhaps diffusional, mechanism by which space exposure affects crystalline material. These observations could alternatively be explained by the occasional bombardment of the lunar surface by solar energetic particles (SEPs), which are substantially more energetic than solar wind ions. Hydrogen SEPs have kinetic energies of 2–10 MeV (Mewaldt et al., 2009), whereas typical solar wind H^+ ions have kinetic energies of ∼1 keV (Gosling et al., 1976). Although SEPs are likely to implant further into lunar soil than average solar wind ions, they occur far less frequently. Without additional support from independent lines of evidence (e.g., observing tracks via TEM), these confounding factors preclude definitive conclusions about the role of SEPs in the weathering of our samples.

5 Conclusions

We used SINS to examine surface-correlated, mid-IR space weathering effects in lunar soil grains. In general, our results are consistent with the spectral changes previously hypothesized to be correlated with the microstructural and compositional changes measured by TEM, but provide crucial information regarding the scale and distribution of the spectral manifestation of ion irradiation and micrometeoroid bombardment. By interrogating space weathering effects with a spatial resolution on the order of the underlying structural and chemical changes in the mineral, we have shown that this technique fills the gap between TEM microstructural studies and far-field FTIR measurements.

The data presented above provide clear evidence in support of previous findings that space weathering effects are the result of highly localized processes (on the order of tens of nanometers). We found that the effect size varies continuously (at the sampled spatial resolution) over a micrometer-scale range of depths. Our results additionally indicate that soil maturity indices should be used with caution when discussing micron-scale sub-samples of lunar soil. While maturity is indicative of large-scale weathering effects, our results reinforce the variability of exposure history among a soil's constituent grains.

The techniques utilized in this study have been shown to produce results in accordance similar to those observed in bulk lunar soils. Taking advantage of techniques with spatial resolutions on the order of tens of nanometers, such as afforded by SINS, may prove useful for studying the relative contribution of each small-scale process (e.g., solar wind implantation, nanophase iron production, micrometeoroid impacts) to the more broad space weathering observations. Spatially-resolved near-field IR data may also be used to inform and refine the techniques used to simulate weathering phenomena in the laboratory. With a more detailed understanding of the spectral effects of charged-particle irradiation on mineral and soil grains, it may also be possible to draw parallels to, among other things, silicate processing in the interstellar medium (Chiar & Tielens, 2006). Detailed studies of the association between specific molecular vibrational modes and the features present in SINS spectra of minerals will shed further light on the mechanisms of space weathering. Information regarding the molecular bonds affected by space weathering, paired with precise chronometry and compositional measurements of weathered lunar soils, may help to constrain or validate current models of space weathering processes.

Acknowledgments

This research used the SINS instrument at beamline 5.4 of the Advanced Light Source, which is a DOE Office of Science User Facility under contract no. DE-AC02-05CH11231.

Data Availability Statement:

The data used for this research will be available at the Digital Research Material Repository at Washington University in St. Louis (citation TBD).

References

Adams, J. B., Hörz, F., & Gibbons, R. V. (1979). Effects of shock-loading on the reflectance spectra of plagioclase, pyroxene, and glass. In *Lunar and Planetary Science Conference* (Vol. 10, p. 1-3). Retrieved from `https://ui.adsabs.harvard.edu/abs/1979LPI....10....1A`

Andrews, D. F. (1974). A robust method for multiple linear regression. *Technometrics*, *16*(4), 523–531. doi: 10.1080/00401706.1974.10489233

Basu, A. (2005). Nanophase Fe^0 in lunar soils. *J. Earth Syst. Sci.*, *114*(3), 375–380. doi: 10.1007/BF02702956

Bechtel, H. A., Muller, E. A., Olmon, R. L., Martin, M. C., & Raschke, M. B. (2014). Ultrabroadband infrared nanospectroscopic imaging. *PNAS (USA)*, *111*(20), 7191–7196. doi: 10.1073/pnas.1400502111

Burgess, K., & Stroud, R. (2018). Phase-dependent space weathering effects and spectroscopic identification of retained helium in a lunar soil grain. *Geochimica et Cosmochimica Acta*, *224*, 64–79. doi: 10.1016/j.gca.2017.12.023

Chiar, J. E., & Tielens, A. G. G. M. (2006). Pixie dust: The silicate features in the diffuse interstellar medium. *ApJ*, *637*(2), 774–785. doi: 10.1086/498406

Chihara, H., & Koike, C. (2017). Infrared absorption spectra of plagioclase feldspar: Dependencies of composition and temperature. *Planetary and Space Science*, *149*, 94–99. doi: 10.1016/j.pss.2017.06.003

Christoffersen, R., Mckay, D. S., & Keller, L. P. (1996). Microstructure, chemistry, and origin of grain rims on ilmenite from the lunar soil finest fraction. *Meteoritics & Planetary Science*, *31*(6), 835–848. doi: 10.1111/j.1945-5100.1996.tb02117.x

Cleveland, W. S. (1979). Robust locally weighted regression and smoothing scatterplots. *Journal of the American Statistical Association*, *74*(368), 829–836. doi: 10.1080/01621459.1979.10481038

Cleveland, W. S., & Devlin, S. J. (1988). Locally weighted regression: An approach to regression analysis by local fitting. *Journal of the American Statistical Association*, *83*(403), 596–610. doi: 10.1080/01621459.1988.10478639

Farrell, W. M., Hurley, D. M., & Zimmerman, M. I. (2015). Solar wind implantation into lunar regolith: Hydrogen retention in a surface with defects. *Icarus*, *255*, 116–126. doi: 10.1016/j.icarus.2014.09.014

Gosling, J. T., Hildner, E., MacQueen, R. M., Munro, R. H., Poland, A. I., & Ross, C. L. (1976). The speeds of coronal mass ejection events. *Solar Physics*, *48*(2), 389–397. doi: 10.1007/bf00152004

Govyadinov, A. A., Mastel, S., Golmar, F., Chuvilin, A., Carney, P. S., & Hillenbrand, R. (2014). Recovery of permittivity and depth from near-field data as a step toward infrared nanotomography. *ACS Nano*, *8*(7), 6911–6921. doi: 10.1021/nn5016314

Hamilton, V. E. (2000). Thermal infrared emission spectroscopy of the pyroxene mineral series. *Journal of Geophysical Research: Planets*, *105*(E4), 9701–9716. doi: 10.1029/1999je001112

Hamilton, V. E. (2003). Thermal infrared emission spectroscopy of titanium-enriched pyroxenes. *Journal of Geophysical Research*, *108*(E8). doi: 10.1029/2003je002052

Hapke, B. (2001). Space weathering from Mercury to the asteroid belt. *JGR: Planets*, *106*(E5), 10039–10073. doi: 10.1029/2000je001338

Hermann, P., Hoehl, A., Ulrich, G., Fleischmann, C., Hermelink, A., Kästner, B., ... Ulm, G. (2014). Characterization of semiconductor materials using synchrotron radiation-based near-field infrared microscopy and nano-FTIR spectroscopy. *Optics Express*, *22*(15), 17948. doi: 10.1364/oe.22.017948

Huth, F., Govyadinov, A., Amarie, S., Nuansing, W., Keilmann, F., & Hillenbrand, R. (2012). Nano-FTIR absorption spectroscopy of molecular fingerprints at 20 nm spatial resolution. *Nano Letters*, *12*(8), 3973–3978. doi: 10.1021/nl301159v

Johnson, J. R., Hörz, F., Lucey, P. G., & Christensen, P. R. (2002). Thermal infrared spectroscopy of experimentally shocked anorthosite and pyroxenite: Implications for remote sensing of Mars. *Journal of Geophysical Research*, *107*(E10). doi: 10.1029/2001JE001517

Johnson, J. R., Hörz, F., & Staid, M. I. (2003). Thermal infrared spectroscopy and modeling of experimentally shocked plagioclase feldspars. *American Mineralogist*, *88*(10), 1575–1582. doi: 10.2138/am-2003-1020

Kaluna, H. M., Ishii, H. A., Bradley, J. P., Gillis-Davis, J. J., & Lucey, P. G.

(2017). Simulated space weathering of Fe- and Mg-rich aqueously altered minerals using pulsed laser irradiation. *Icarus*, *292*, 245–258. doi: 10.1016/j.icarus.2016.12.028

Keller, L. P., & McKay, D. S. (1993). Discovery of vapor deposits in the lunar regolith. *Science*, *261*(5126), 1305–1307. doi: 10.1126/science.261.5126.1305

Keller, L. P., & McKay, D. S. (1997). The nature and origin of rims on lunar soil grains. *Geochimica et Cosmochimica Acta*, *61*(11), 2331–2341. doi: 10.1016/S0016-7037(97)00085-9

Lantz, C., Brunetto, R., Barucci, M. A., Fornasier, S., Baklouti, D., Bourçois, J., & Godard, M. (2017). Ion irradiation of carbonaceous chondrites: A new view of space weathering on primitive asteroids. *Icarus*, *285*, 43–57. doi: 10.1016/j.icarus.2016.12.019

Lucey, P. G., & Noble, S. K. (2008). Experimental test of a radiative transfer model of the optical effects of space weathering. *Icarus*, *197*(1), 348–353. doi: 10.1016/j.icarus.2008.05.008

Lucey, P. G., & Riner, M. A. (2011). The optical effects of small iron particles that darken but do not redden: Evidence of intense space weathering on Mercury. *Icarus*, *212*(2), 451–462. doi: 10.1016/j.icarus.2011.01.022

Makreski, P., Jovanovski, G., Gajović, A., Biljan, T., Angelovski, D., & Jaćimović, R. (2006). Minerals from Macedonia. XVI. Vibrational spectra of some common appearing pyroxenes and pyroxenoids. *Journal of Molecular Structure*, *788*(1-3), 102–114. doi: 10.1016/j.molstruc.2005.11.024

Mewaldt, R. A., Leske, R. A., Stone, E. C., Barghouty, A. F., Labrador, A. W., Cohen, C. M. S., ... Wiedenbeck, M. E. (2009). *STEREO* observations of energetic neutral hydrogen atoms during the 2006 December 5 solar flare. *The Astrophysical Journal*, *693*(1), L11–L15. doi: 10.1088/0004-637x/693/1/l11

Morris, R. V. (1978). The surface exposure (maturity) of lunar soils: Some concepts and I_S/FeO compilation. In *Lunar and Planetary Science Conference* (Vol. 9, pp. 2287–2297).

Nash, D., & Salisbury, J. (1991). Infrared reflectance spectra (2.2–15 µm) of plagioclase feldspars. *Geophysical Research Letters*, *18*(6), 1151–1154. doi: 10.1029/91gl01008

Nash, D. B., Salisbury, J. W., Conel, J. E., Lucey, P. G., & Christensen, P. R. (1993). Evaluation of infrared emission spectroscopy for mapping the moon's surface composition from lunar orbit. *Journal of Geophysical Research*, *98*(E12), 23535. doi: 10.1029/93je02604

Noble, S. K., Keller, L. P., & Pieters, C. M. (2005). Evidence of space weathering in regolith breccias I: Lunar regolith breccias. *MAPS*, *40*(3), 397–408. doi: 10.1111/j.1945-5100.2005.tb00390.x

Noble, S. K., Pieters, C. M., & Keller, L. P. (2007). An experimental approach to understanding the optical effects of space weathering. *Icarus*, *192*(2), 629–642. doi: 10.1016/j.icarus.2007.07.021

Noguchi, T., Kimura, M., Hashimoto, T., Konno, M., Nakamura, T., Zolensky, M. E., ... Ishibashi, Y. (2014). Space weathered rims found on the surfaces of the Itokawa dust particles. *Meteoritics and Planetary Science*, *49*(2), 188–214. doi: 10.1111/maps.12111

Noguchi, T., Nakamura, T., Kimura, M., Zolensky, M. E., Tanaka, M., Hashimoto, T., ... Okazaki, R. (2011). Incipient space weathering observed on the surface of Itokawa dust particles. *Science*, *333*(6046), 1121–1125. doi: 10.1126/science.1207794

Pieters, C., Fischer, E., Rode, O., & Basu, A. (1993). Optical effects of space weathering: The role of the finest fraction. *Journal of Geophysical Research*, *98*(E11), 20817. doi: 10.1029/93JE02467

Pieters, C., Taylor, L., Noble, S., Keller, L., Hapke, B., Morris, R., ... Wentworth, S. (2000). Space weathering on airless bodies: Resolving a mystery with lunar

samples. *MAPS*, *35*(5), 1101–1107. doi: 10.1111/j.1945-5100.2000.tb01496.x

Pollard, B., Maia, F. C. B., Raschke, M. B., & Freitas, R. O. (2015). Infrared vibrational nanospectroscopy by self-referenced interferometry. *Nano Letters*, *16*(1), 55–61. doi: 10.1021/acs.nanolett.5b02730

Rhodes, J., & Blanchard, D. (1982). Apollo 11 breccias and soils: aluminous mare basalts or multi-component mixtures? *Lunar and Planetary Science Conference*, *12*, 607–620.

Ross, M., Bence, A. E., Dwornik, E. J., Clark, J. R., & Papike, J. J. (1970). Mineralogy of the lunar clinopyroxenes, augite and pigeonite. *Geochim. Cosmochim. Acta Suppl.*, *1*, 839.

Taylor, L. A., Pieters, C., Patchen, A., Taylor, D.-H. S., Morris, R. V., Keller, L. P., & McKay, D. S. (2010). Mineralogical and chemical characterization of lunar highland soils: Insights into the space weathering of soils on airless bodies. *Journal of Geophysical Research*, *115*(E2), E02002. doi: 10.1029/2009JE003427

Taylor, L. A., Pieters, C. M., Keller, L. P., Morris, R. V., & McKay, D. S. (2001). Lunar mare soils: Space weathering and the major effects of surface-correlated nanophase Fe. *Journal of Geophysical Research: Planets*, *106*(E11), 27985–27999. doi: 10.1029/2000JE001402

Thompson, C. S., & Wadsworth, M. E. (1957). Determination of the composition of plagioclase feldspars by means of infrared spectroscopy. *American Mineralogist*, *42*(5-6), 334–341.

Thompson, M. S., Loeffler, M. J., Morris, R. V., Keller, L. P., & Christoffersen, R. (2019). Spectral and chemical effects of simulated space weathering of the Murchison CM2 carbonaceous chondrite. *Icarus*, *319*, 499–511. doi: 10.1016/j.icarus.2018.09.022

Tucker, O. J., Farrell, W. M., Killen, R. M., & Hurley, D. M. (2019). Solar wind implantation into the lunar regolith: Monte Carlo simulations of H retention in a surface with defects and the H^2 exosphere. *Journal of Geophysical Research: Planets*, *124*(2), 278–293. doi: 10.1029/2018je005805

Wohlfarth, K. S., Wöhler, C., & Grumpe, A. (2019). Space weathering and lunar OH/H_2O — insights from ab initio Mie modeling of submicroscopic iron. *The Astronomical Journal*, *158*(2), 80. doi: 10.3847/1538-3881/ab26af

Xu, X. G., Rang, M., Craig, I. M., & Raschke, M. B. (2012). Pushing the sample-size limit of infrared vibrational nanospectroscopy: From monolayer toward single molecule sensitivity. *The Journal of Physical Chemistry Letters*, *3*(13), 1836–1841. doi: 10.1021/jz300463d